J Mater Sci: Mater Electron (2017) 28:2141–2146
DOI 10.1007/s10854-016-5778-5

Hydrothermal synthesis, optical and magnetic properties of CeO_2 nanosheets with some cracks in their wafery centre

Xiaofei Niu[1] · **Furong Tu**[1]

Received: 13 July 2016 / Accepted: 1 October 2016 / Published online: 7 October 2016

Abstract The polygonal CeO_2 nanosheets have been successfully synthesized by a facile hydrothermal technique. XRD, SEM, TEM, XPS, Raman scattering, photoluminescence (PL) spectra, and *M–H* curve were employed to characterize the samples. The results showed that there are Ce^{3+} ions and oxygen vacancies in the surface of CeO_2 nanosheets with a cubic fluorite structure. It is found that the polygonal nanosheets of 0.5–1.5 µm in diameters and about 50 nm in thickness display a wafery centre with some cracks. The magnetic and photoluminescence measurements indicated that the CeO_2 nanosheets exhibit excellent ferromagnetism and optical properties at room temperature, which is likely attributed to the effects of the Ce^{3+} ions and oxygen vacancies.

1 Introduction

In recent years, nano/microstructures with well-defined shapes and architectures have attracted considerable interest because their physical and chemical properties are closely associated with their geometrical factors such as size, dimensionality, morphology, and orientation [1–4]. Thus, various methods, including hydrothermal synthesis [5], coprecipitation [6], sol–gel [7], thermal evaporation [8], have been widely utilized for the fabrication of CeO_2 with various morphologies and sizes. Since graphene was discovered in 2004 [9] and its discovery was awarded with the Nobel Prize in Physics in 2010, much more consideration has been given to synthesize metal oxides with two-dimensional (2D) nanostructures and to investigate their novel applications, due to their unusual properties derived from their high surface-to-volume ratio, high crystallinity, potential quantum size effects and well-defined chemical composition as well as extremely high anisotropy with an ultrathin thickness [10–13].

As a typical kind of rare earth oxide, CeO_2 has been the subject of intense interest because of its unique properties, including abundant oxygen vacancy defects, high oxygen storage capacity and ability to uptake and release oxygen via the transformation between Ce^{3+} and Ce^{4+}. On account of these characteristics, CeO_2 has been widely used for three-way catalysts (TWC) for the elimination of vehicle exhaust gases [14], ultraviolet (UV) blocking materials [15], photocatalysts for water oxidation [16], oxygen sensors [13] and oxygen ion conductors in solid oxide fuel cells [17]. Although remarkable progress has been made in the synthesis of CeO_2 nanomaterials with various morphologies [18–20], the synthesis of 2D CeO_2 structure is rarely reported. Unlike the synthesis of spherical particles and the one-dimension nanorods/nanowires, the control of crystal growth in two dimensions has been shown to be much more difficult, especially in solution-phase. It is a serious obstacle to synthesize free-standing CeO_2 nanosheets in solution-phase, because CeO_2 with the cubic structure has no intrinsic driving force for anisotropic growth in aqueous routes. Therefore, the fabrication of CeO_2 with 2D structure in solution-phase still remains a great challenge.

In this work, we report the synthesis, excellent optical and magnetic properties of CeO_2 nanosheets via a smart hydrothermal technology. Our method is an effective approach to controlling CeO_2 morphology and size and it is

---

✉ Xiaofei Niu
szniuxf0123@126.com

[1] Anhui Key Laboratory of Spintronics and Nanomaterials Research, Suzhou University, Suzhou 234000, Anhui, People's Republic of China

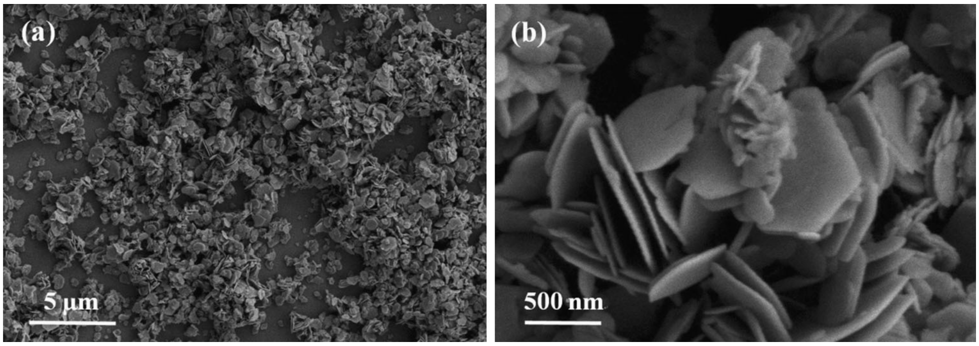

Fig. 1 SEM images of (**a**, **b**) the as-synthesized CeO_2 nanosheets at 160 °C for 36 h

anticipated that this work can shed new light on the synthesis and self-assembly of other nanostructures.

2 Experimental

2.1 Material preparation

All the reagents were of analytical grade purity and used as received without further purification before the synthesized process. A typical synthetic procedure is as follows: firstly, 4 mmol $CeCl_3 \cdot 7H_2O$ and 60 mmol NH_4HCO_3 were dissolved in 10 and 20 mL deionized water with vigorous magnetic stirring at room temperature respectively. Then, 20 mL NH_4HCO_3 aqueous solution was slowly added to 10 mL $CeCl_3 \cdot 7H_2O$ aqueous solution under continuous stirring and the white precipitate and a lot of bubbles were generated immediately. Subsequently, the white suspension promptly turned yellow after dropwise addition of 5 mL ethylenediamine. After continuous stirring for 0.5 h, the suspending solution was immediately transferred into a 50 ml Teflon-lined autoclave and heated at 160 °C for 36 h, followed by natural cooling to room temperature. The fresh precipitates were washed with distilled water and ethanol three times in turn before drying at 80 °C for overnight. Finally, the samples were calcined in air at 500 °C for 5 h.

2.2 Characterization

The powder X-ray diffraction (XRD) patterns of the products were obtained by an X-ray diffractometer (XRD, XD-3) using Cu Kα radiation ($\lambda = 0.154$ nm). Morphology and size of the products were observed by scanning electron microscope (SEM, S-4800, Japan) and transmission electron microscope (TEM, JEM-2100, Japan). Elemental bonding valence was achieved by X-ray photoelectron microscopy (XPS, ESCALAB 250 US Thermo Electron Co). The Raman spectrum was recorded by a Raman spectrometer system (inVia-Reflex) using a laser with 532 nm excitation at room temperature. Photoluminescent (PL) emission spectrum was determined by a fluorescence spectrophotometer (Hitachi F-4500) using excitation light of 330 nm. The *M–H* curve was measured at room temperature by a vibrating sample magnetometer (BHV-55).

3 Results and discussion

3.1 Morphology characterization

The morphologies and sizes of synthesized products were studied by scanning electron microscope (SEM) and transmission electron microscope (TEM). Figure 1a, b shows the SEM images of the CeO_2 samples synthesized at 160 °C for 36 h. It can be seen that there are a large amount of polygonal nanosheets of 0.5–1.5 µm in diameters and about 50 nm in thickness, as shown in Fig. 1a, b. From Fig. 2a, the polygonal nanosheets display a wafery centre with some cracks. The selected area electron diffraction (SAED) pattern (inset of Fig. 3a) indicates that each nanosheet is a monocrystalline material. Figure 2b shows a high-resolution TEM (HRTEM) image. The clear lattice fringes with interplanar spacing of 0.322 nm can be assigned to the CeO_2 {111} crystal plane and there are some defects in the nanosheets (marked with a red rectangle).

3.2 Structure characterization

A typical diffraction pattern of the as-obtained CeO_2 products is illustrated in Fig. 3. All of the peaks could be exactly indexed to the phase of CeO_2 with a cubic fluorite structure, being in good agreement with the JCPDS file for CeO_2 ($Fm\bar{3}m$, JCPDS No. 43-1002). The sharp diffraction peaks suggest a high degree of crystallinity of synthesized samples. It is noticed that no signals of impurities were seen in Fig. 3, indicating the high purity of the samples. The relative intensity between characteristic peaks at about 2θ: 28.5, 33.1, 47.4 and 56.2 do not change clearly, which assigned to the crystal planes (1 1 1), (2 0 0), (2 2 0) and

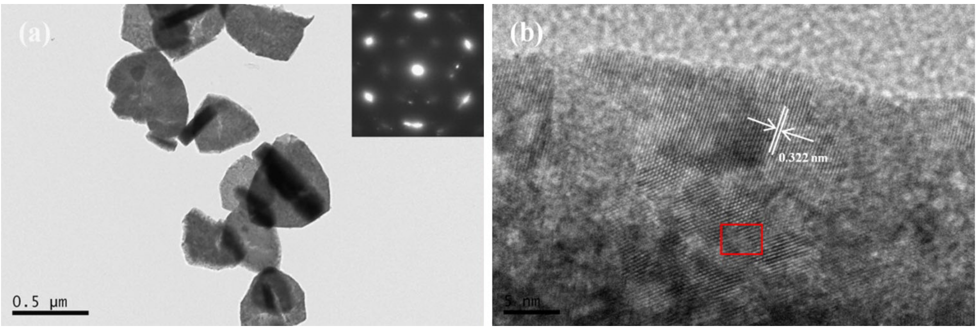

Fig. 2 **a** TEM image of CeO_2 nanosheets synthesized at 160 °C for 36 h and the *inset* is SAED pattern, **b** HRTEM image of the CeO_2 nanosheets

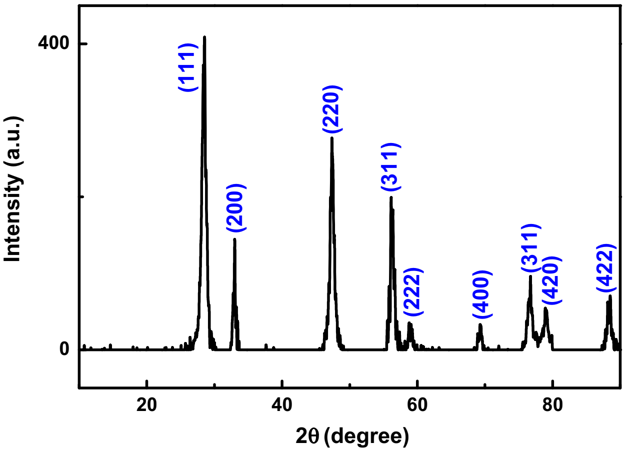

Fig. 3 XRD pattern of the CeO_2 nanosheets synthesized at 160 °C for 36 h

(3 1 1) respectively, suggesting that there is no preferred orientation or orientation crystal growth.

3.3 Composition and chemical state

To further study the tunability of the surface properties, XPS analysis was carried out to investigate the surface composition and chemical state of the nanosheets synthesized at 160 °C for 36 h. As we all know, due to the highly non-stoichiometric nature, there are two different oxidation states for elemental Ce in CeO_2, namely, Ce(III) and Ce(IV). The Ce 3d spectra and corresponding peak fitted deconvolutions are given in Fig. 4a. The peaks located in 916.19, 908.14, 899.50, 898.08, 888.17 and 882.69 eV are attributed to $3d_{3/2}$ and $3d_{5/2}$ for Ce^{4+} final states [21], while those at 900.34 and 883.27 eV are the present for $3d_{3/2}$ and $3d_{5/2}$ for Ce^{3+} 3d final states [22]. This result indicates that the main valence of cerium in the sample was +4, and a small amount of Ce^{3+} distributes around oxygen vacancies on the CeO_2 surfaces [23], regardless of the valences of the starting cerium salts. However, in order to maintain the particles in an electrically neutral state, the lattice oxygen would escape from the structure and finally result in the formation of intrinsic oxygen vacancies [3]. From Fig. 4b, three BE peaks at binding energy 529.20, 530.23 and 530.95 eV can be clearly identified, which can be assigned to lattice oxygen ions in CeO_2, absorbed oxygen and lattice oxygen ions in Ce_2O_3 [24–26], respectively. XPS spectra confirmed the high chemical purity of the CeO_2 nanoparticles consisting solely of Ce and O.

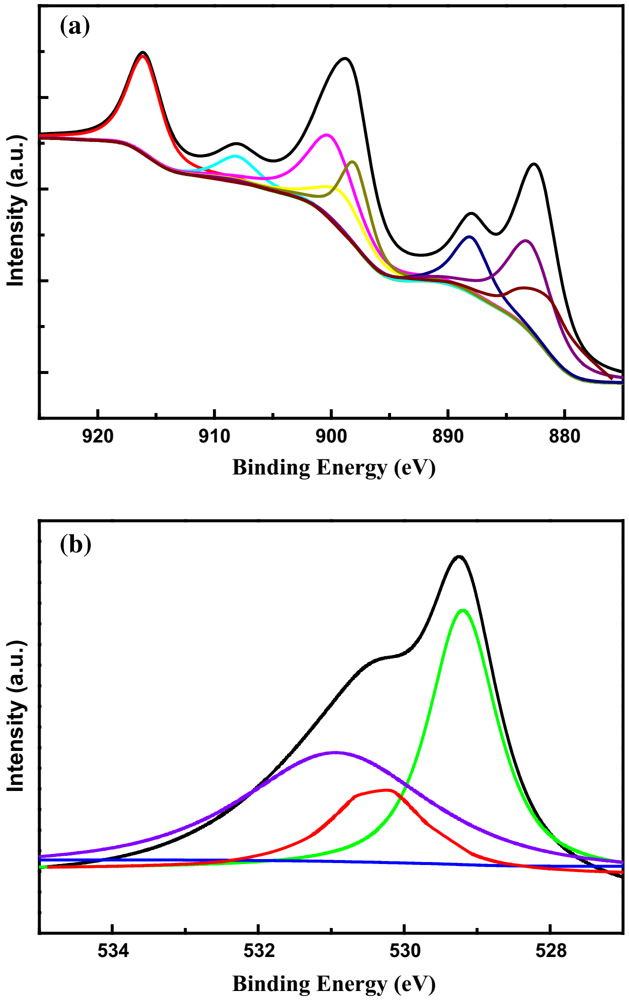

Fig. 4 XPS cores level spectra of Ce3d (**a**) and O1s (**b**) of CeO_2 nanosheets obtained at 160 °C for 36 h

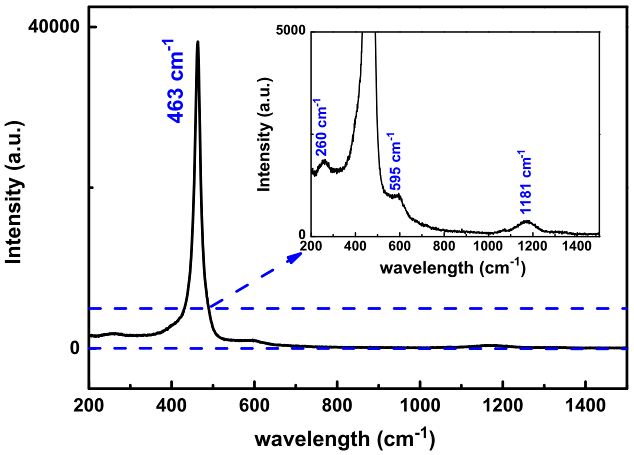

Fig. 5 Room temperature Raman spectra of CeO_2 nanosheets synthesized at 160 °C for 36 h

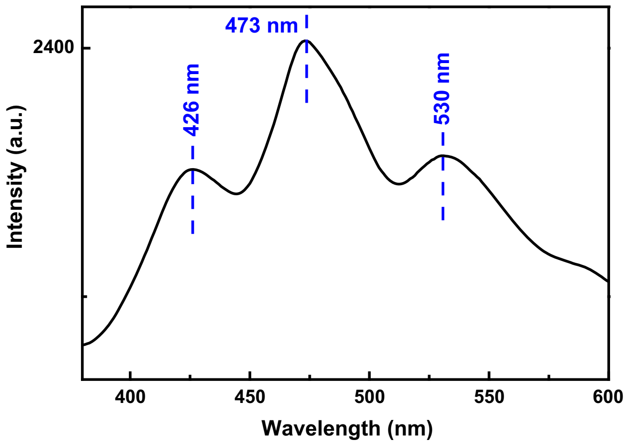

Fig. 6 Photoluminescence spectrum of CeO_2 nanosheets synthesized at 160 °C for 36 h

3.4 Optical properties

Raman spectroscopy is considered to be a very facile and nonvolatile technique for characterization of CeO_2 nanoparticles. Therefore, to better understand the defects in the CeO_2 nanosheets, the Raman scattering was carried out and is shown in Fig. 5. As we have seen, the strong Raman peak centered at about 463 cm^{-1}, corresponding to the triply degenerate F_{2g} mode of the fluorite crystal structure of CeO_2 and it can be considered as the symmetric stretching mode of oxygen atoms around cerium ions, and the molecule retains its tetrahedral symmetry throughout [27]. Because once the O atoms move, the vibrational mode is nearly independent of the cation mass [28]. Therefore, the peak should be very sensitive to any disorder in the oxygen sublattice resulting from thermal, doping, or grain size [29]. However, this main peak of CeO_2 nanosheets shifts toward lower wavenumber comparing to bulk one (465 cm^{-1}) and becomes more asymmetric, several factors, such as phonon confinement, increased lattice strain, nonuniform strain and variations in phonon relaxation may account for the changes [24]. It is likely that Ce^{3+} ions and oxygen vacancies in the samples are responsible for the changes in the Raman peak position and linewidth of the 463 cm^{-1} peak. In addition, the low intense peak at 260 cm^{-1} is assigned to the disorder in the system [30], while another weak and less prominent band near 595 cm^{-1} is attributed to defect spaces which include oxygen vacancies [31]. In fact, the introduction of oxygen vacancies or increasing the concentration at the surface of CeO_2 samples can inhibit the recombination of electron–hole pairs to improve their performance as efficient photocatalysts [26]. Finally, the peak near 1181 cm^{-1} is ascribed to the second-order Raman mode of surface superoxide species (O_2^-), and has little additional contributions from F_{2g} symmetry [32].

The oxygen ions are not closely packed in the CeO_2 with a cubic fluorite structure. Therefore, many oxygen vacancies arise for maintaining the basic fluorite structure of CeO_2 [33]. The photoexcitation process in CeO_2 is described by Kroger–Vink notation given by [34]

$$4Ce_{Ce} + O_O \rightarrow 2Ce_{Ce} + 2Ce^{x}_{Ce} + V_{O}^{\cdot\cdot} + (1/2)O_2(g) \qquad (1)$$

All the symbols have the following meaning; Ce_{Ce} and Ce^{x}_{Ce} are Ce^{4+} and Ce^{3+} ions on a Ce lattice site, respectively, O_O is O^{2-} ion on an O lattice site, and $V_{O}^{\cdot\cdot}$ is neutral oxygen vacancy site. In other words, photoluminescence in CeO_2 arises due to strong light absorption through the charge transfer between O^{2-} and Ce^{4+}. As is well-known that CeO_2 is a wide band semiconductor, the electron transition from the valence band to Ce 4f level is easy due to the Ce 4f energy level with 1.2 eV width, which localizes at the forbidden band and lies about 3 eV above the valence band (O 2p) [2]. When the electronic transition takes place, the excited electrons will populate Ce 4f as well as vacant spaces of oxygen defects [35]. Moreover, the oxygen defect states are present just below Ce 4f level. Therefore, the wider emission bands are observed due to there are many defects energy levels localise between Ce 4f and O 2p level. Figure 6 shows the PL spectra of CeO_2 nanosheets measured at room temperature at an excitation wavelength of 330 nm. It can be seen that the CeO_2 samples show a strong PL emission single at 473 nm, and two weaker peaks are mainly peaked at ~426 and 530 nm. The investigation showed that the emission bands ranging from 400 to 500 nm for CeO_2 sample are attributed to the hopping from different defect levels to valence band, and can be partly certificated by comparing the relationship of

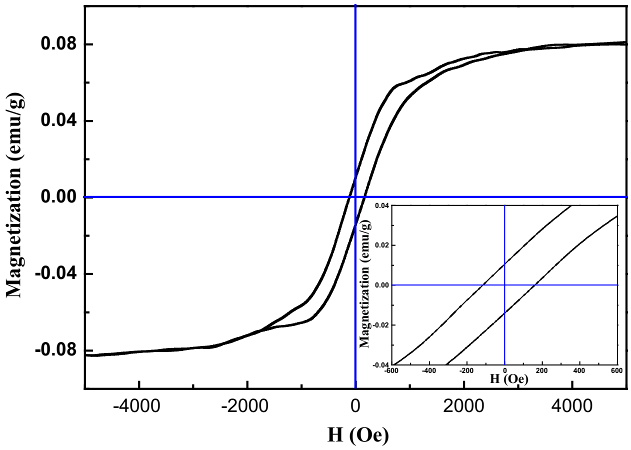

Fig. 7 *M–H* curve of CeO_2 nanosheets synthesized at 160 °C for 36 h and the *inset figure* presents the spectra in a suitable scale

peak intensity and band gap [24, 31, 36]. Among them, the strong emission of the CeO_2 nanoparticles at 473 nm is related to the abundant defects such as dislocations (shown in Fig. 2b, marked with a red rectangle), which is helpful for fast oxygen transportation. Another weak emission band centred on 532 nm may be attributed to the oxygen vacancies in the crystal with defect energy levels below the Ce 4f band [37]. As we know that defects have an important influence on the chemical and physical properties of CeO_2 nanocrystals, including oxygen transportation, catalysts, fuel cells, and so on.

3.5 Ferromagnetism analysis

The magnetic properties of the CeO_2 nanosheets synthesized at 160 °C for 36 h were characterized by measuring the field dependence of magnetization at room temperature. Figure 7 shows the *M–H* curve of CeO_2 nanosheets at room temperature and the inset of Fig. 7 is the magnetization of the central part. As we can see that the samples exhibit a very well defined hysteresis loop and the saturation magnetization (M_s) is 0.08 emu/g, the residual magnetization (M_r) is 0.01 emu/g and the coercivity (H_c) is 163 Oe. It is noteworthy that the value of M_s are larger than those previous reports in which the pure CeO_2 [38, 39] and CeO_2 nanoparticles were doped with magnetic element, such as Ni, Co and Cu [40–42]. Base on those reports, it can be concluded that magnetic not only from doped elements, but a part of CeO_2 itself becomes magnetic, although bulk CeO_2 with a face-centered cubic structure is paramagnetic. Firstly, from theoretical and experimental studies, oxygen vacancies were supposed to give rise to the RTFM. Bernardi et al. [43] has confirmed that the presence of substantial oxygen vacancies would lead to magnetic order. Secondly, based on the results of XPS and Raman analyses, there were Ce^{3+} and oxygen vacancy in the surface of CeO_2 samples. The electron orbits (Ce^{4+}–O^{2-}–Ce^{3+}) are no longer symmetrical and an uncoupled spins in the Ce 4f orbit are generated. Therefore, the RTFM might consequently arises from a nearest-neighbor interaction: double exchange (Ce^{4+}–O^{2-}–Ce^{3+}) [44]. Wang et al. [45] believed that the FM of CeO_2 samples is related to the concentration of Ce^{3+} and oxygen deficiencies. To sum up, the RTFM of the CeO_2 nanosheets can be attributed to the effects of Ce^{3+} ions and oxygen vacancies.

4 Conclusions

The polygonal CeO_2 nanosheets with the thickness of 50 nm were successfully prepared by a simple hydrothermal method. The method of synthetic is effective and reproducible and can shed new light on the fabrication of other rare-earth morphology-controlled inorganic nanomaterials. X-ray diffraction (XRD) inferred that the synthesized CeO_2 nanosheets exhibited a fluorite cubic structure. The transmission electron microscope (TEM) revealed that almost all the polygonal nanosheets have a wafery centre with some cracks. X-ray photoelectron spectroscopy (XPS) and the Raman spectroscopy reflected the existence of the oxygen vacancies and Ce^{3+} ions in the surface of CeO_2 nanosheets. The as-synthesized CeO_2 samples showed excellent optical and magnetic properties, which can be reasonably explained for the influences of oxygen vacancies and Ce^{3+} ions. Consequently, the polygonal CeO_2 nanosheets are promising material for practical applications in related areas.

Acknowledgments This work was supported by the National Natural Science Foundation of China (Nos. 51072002, 51272003), Coal mine machinery and electronic engineering research Center of Suzhou University (2014YKF16), Outstanding Young Talents Funded Projects of Suzhou University (Grant No. 2014XQNRL010), and the Natural Science Research Fund of Anhui Provincial Department of Education (KJ2016A775).

References

1. Y.B. Zeng, Z.Q. Li, Y.F. Liang, X.Q. Gan, M.M. Zheng, Inorg. Chem. **52**, 9590 (2013)
2. L.N. Wang, F.M. Meng, K.K. Li, F. Lu, Appl. Surf. Sci. **286**, 269 (2013)
3. B. Xu, Q.T. Zhang, S.S. Yuan, M. Zhang, T. Ohno, Chem. Eng. J. **260**, 126 (2015)
4. R.C. Rao, M. Yang, C.S. Li, H.Z. Dong, S. Fang, A.M. Zhang, J. Mater. Chem. A **3**, 782 (2015)
5. F.M. Meng, L.N. Wang, J.B. Cui, J. Alloys Compd. **556**, 102 (2013)
6. S. Letichevsky, C.A. Tellez, R.R.D. Avillez, M.I.P.D. Silva, M.A. Fraga, L.G. Appel, Appl. Catal. B Environ. **58**, 203 (2005)
7. H.Y. Xiao, Z.H. Ai, L.Z. Zhang, J. Phys. Chem. C **113**, 16625 (2009)

8. C. Paun, O.V. Safonova, J. Szlachetko, P.M. Abdala, M. Nachtegaal, J. Sa, E. Kleymenov, A. Cervellino, F. Krumeich, J.A.V. Bokhoven, J. Phys. Chem. C **116**, 7312 (2012)
9. K.S. Novoselov, A.K. Geim, S.V. Morozov, D. Jiang, Y. Zhang, S.V. Dubonos, I.V. Grigorieva, A.A. Firsov, Science **306**, 666 (2004)
10. R.R. Cui, W.C. Lu, L.M. Zhang, B.H. Yue, S.S. Shen, J. Phys. Chem. C **113**, 21520 (2009)
11. J. Zhang, H. Kumagai, K. Yamamura, S. Ohara, S. Takami, A. Morikawa, H. Shinjoh, K. Kaneko, T. Adschiri, A. Suda, Nano Lett. **11**, 361 (2011)
12. L.H. Jiang, M.G. Yao, B. Liu, Q.J. Li, R. Liu, Z. Yao, S.C. Lu, W. Cui, X. Hua, B. Zou, T. Cui, B.B. Liu, CrystEngComm **15**, 3739 (2013)
13. N. Izu, T. Itoh, M. Nishibori, I. Matsubara, W. Shin, Sens. Actuators B Chem. **171**, 350 (2012)
14. D.S. Zhang, X.J. Du, L.Y. Shi, R.H. Gao, Dalton Trans. **41**, 14455 (2012)
15. R.J. Qi, Y.J. Zhu, G.F. Cheng, Y.H. Huang, Nanotechnology **16**, 2502 (2005)
16. J. Qi, K. Zhao, G.D. Li, Y. Gao, H.J. Zhao, R.B. Yu, Z.Y. Tang, Nanoscale **6**, 4072 (2014)
17. Z.L. Zhan, S.A. Bamett, Science **308**, 844–847 (2005)
18. X.Y. Yang, X. Gao, Y.L. Gan, C.Y. Gao, X.L. Zhang, K. Ting, B.M. Wu, Z.R. Gou, J. Phys. Chem. C **114**, 6265 (2010)
19. Y. Chen, C. Qiu, C. Chen, X. Fan, S. Xu, W. Guo, Z. Wang, Mater. Lett. **122**, 90 (2014)
20. X.H. Lu, D.Z. Zheng, J.Y. Gan, Z.Q. Liu, C.L. Liang, P. Liu, Y.X. Tong, J. Mater. Chem. **20**, 7118 (2010)
21. C.R. Li, M.Y. Cui, Q.T. Sun, W.J. Dong, Y.Y. Zheng, K. Tsukamoto, B.Y. Chena, W.H. Tang, J. Alloys Compd. **504**, 498 (2010)
22. N.S. Ferreira, R.S. Angélica, V.B. Marques, C.C.O. de Lima, M.S. Silva, Mater. Lett. **165**, 139 (2016)
23. W. Gao, Z.Y. Zhang, J. Li, Y.Y. Ma, Y.Q. Qu, Nanoscale **7**, 11686 (2015)
24. F.M. Meng, J.F. Gong, Z.H. Fan, H.J. Li, J.T. Yuan, Ceram. Int. **42**, 4700 (2016)
25. F.L. Liang, Y. Yu, W. Zhou, X.Y. Xu, Z.H. Zhu, J. Mater. Chem. A **3**, 634 (2015)
26. A. Younis, D. Chu, Y.V. Kaneti, S. Li, Nanoscale **8**, 378 (2016)
27. H. Li, A. Petz, H. Yan, J.C. Nie, S. Kunsagi-Mate, J. Phys. Chem. C **115**, 1480 (2011)
28. H.R. Tan, J.P.Y. Tan, C. Boothroyd, T.W. Hansen, Y.L. Foo, M. Lin, J. Phys. Chem. C **116**, 242 (2012)
29. A.C. Cabral, L.S. Cavalcante, R.C. Deus, E. Longo, A.Z. Simões, F. Moura, Ceram. Int. **40**, 4445 (2014)
30. J. Zdravković, B. Simović, A. Golubović, D. Poleti, I. Veljković, M. Šćepanović, G. Branković, Ceram. Int. **41**, 1970 (2015)
31. C. Zhang, F.M. Meng, L.N. Wang, M. Zhang, Z.L. Ding, Mater. Lett. **130**, 202 (2014)
32. H.F. Xu, H. Li, J. Magn. Magn. Mater. **377**, 272 (2015)
33. T. Masui, K. Fujiwara, K.I. Machida, G.Y. Adachi, Chem. Mater. **9**, 2197 (1997)
34. E. Shoko, M.F. Smith, R.H. McKenzie, J. Phys, Condens. Mater. **22**, 223201 (2010)
35. B. Choudhury, A. Choudhury, Mater. Chem. Phys. **131**, 666 (2012)
36. S. Phoka, P. Laokul, E. Swatsitang, V. Promarak, S. Seraphin, S. Maensiri, Mater. Chem. Phys. **115**, 423 (2009)
37. G.F. Wang, Q.Y. Mu, T. Chen, Y.D. Wang, J. Alloys Compd. **493**, 202 (2010)
38. S.Y. Chen, Y.H. Lu, T.W. Huang, D.C. Yan, C.L. Dong, J. Phys. Chem. C **114**, 19576 (2010)
39. J.H. Chen, Y.J. Lin, H.C. Chang, Y.H. Chen, L. Horng, C.C. Chang, J. Alloys Compd. **548**, 235 (2013)
40. A. Thurber, K.M. Reddy, V. Shutthanandan, M.H. Engelhard, C. Wang, J. Hays, A. Punnoose, Phys. Rev. B **76**, 165206 (2007)
41. A. Tiwari, V.M. Bhosle, S. Ramachandran, N. Sudhakar, J. Narayan, S. Budak, A. Gupta, Appl. Phys. Lett. **88**, 142511 (2006)
42. P. Slusser, D. Kumar, A. Tiwari, Appl. Phys. Lett. **96**, 142506 (2010)
43. M.I.B. Bernardi, A. Mesquita, F. Beron, K.R. Pirota, AOd Zevallos, A.C. Doriguetto, H.B.D. Carvalho, Phys. Chem. Chem. Phys. **17**, 3072 (2015)
44. S.Y. Chen, C.H. Tsai, M.Z. Huang, D.C. Yan, T.W. Huang, A. Gloter, C.L. Chen, H.J. Lin, C.T. Chen, C.L. Dong, J. Phys. Chem. C **116**, 8707 (2012)
45. L.N. Wang, F.M. Meng, Mater. Res. Bull. **48**, 3492 (2013)